Investigation of Charge Transfer Kinetics in Multilayer PEO/LLZO Solid-State Batteries

Bryce A. Tappan, Katrin Geng,[°] Daniele Vivona,[°] Daniel Wang, David Mankus, Abigail Lytton-Jean, Dominic Bresser, and Yang Shao-Horn[*]

ABSTRACT: Lithium−metal batteries employing solid electrolytes (ceramics or polymers) could surpass the energy and power densities of current state-of-the-art lithium-ion batteries. Unfortunately, ceramic electrolyte/electrode interfaces suffer from poor interfacial contact, and polymer electrolytes show insufficient ionic conductivities for practical uses. Composite solid electrolytes, comprised of mixtures of ceramic and polymer electrolytes, could mitigate these challenges by combining high ionic conductivity with good interfacial contact. However, it is imperative to understand the kinetics of charge transfer at interfaces in composite solid electrolytes, as these can drastically affect the overall ion transport properties of such electrolytes. Here, we design a systematic study of charge transfer kinetics using multilayer LLZO/PEO (tantalum-doped lithium lanthanum zirconium oxide and poly(ethylene oxide)) solid electrolyte architectures as model systems for composite electrolytes. Electrochemical impedance spectroscopy and DC polarization measurements highlight the nonlinear charge transfer kinetics at Li/PEO as well as PEO/LLZO interfaces and show that charge transfer kinetics at each of these interfaces is limited by ion transfer in accordance with a Butler−Volmer model that incorporates a film resistance term. In addition, slow ion transport through the solid electrolyte interphase at Li/PEO interfaces and through contamination layers at LLZO/PEO interfaces are dominant sources of impedance, the latter of which can be significantly mitigated by decreasing interfacial contaminants through a high-temperature (700 °C) heat treatment of LLZO prior to battery assembly. These results provide new insights into the charge transfer kinetics at interfaces in multilayer and composite solid-state batteries and support the future design thereof.

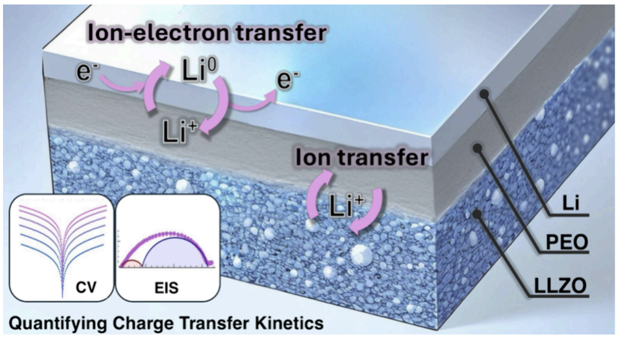

KEYWORDS: *Charge transfer kinetics, solid-state batteries, ceramic electrolytes, polymer electrolytes, lithium metal batteries, impedance spectroscopy, cyclic voltammetry*

INTRODUCTION

Solid-state batteries that couple ceramic and/or polymer electrolytes with lithium metal anodes and high-voltage cathodes may yield practically achievable energy densities of ≥ 500 Wh kg^{-1}, surpassing energy densities of current state-of-the-art lithium-ion batteries (∼260 Wh kg^{-1}).[1−5] Moreover, solid electrolytes such as $Li_7La_3Zr_2O_{12}$ (LLZO) can have fast interfacial kinetics with lithium metal with exchange current densities up to at least several hundred mA cm^{-2} (corresponding to area-specific impedance on the order of ∼0.1 Ω cm^2) at room temperature,[6−9] which is significantly faster than those of liquid or polymer electrolytes,[10−12] and may thereby enable fast (dis)charging at the anode interface with minimal Ohmic loss due to charge transfer resistance. The rapid rates of interfacial ion and electron transfer at Li/LLZO interfaces are reflected in linear DC polarization responses over wide potential windows,[3,6,13] where the rate limiting step is the transport of ions through the bulk of the electrolyte. Unfortunately, solid-state batteries employing ceramic electrolytes are hindered by poor interfacial contact between the lithium metal anode and the solid electrolyte. Contact issues of this nature persist even when stack pressures in excess of tens of MPa are applied to the solid-state battery cells,[9,14] causing poor cell performance due to constriction impedances at the interface, as well as inhomogeneous lithium stripping and plating that can lead to growth of Li dendrites through the solid electrolyte.[15−17]

Polymer electrolytes such as poly(ethylene oxide) (PEO) with dissolved lithium salts are attractive alternatives to ceramic electrolytes in that their low shear modulus and flexibility can facilitate better electrolyte/electrode contact in solid-state batteries.[18−21] However, not only do polymer electrolytes

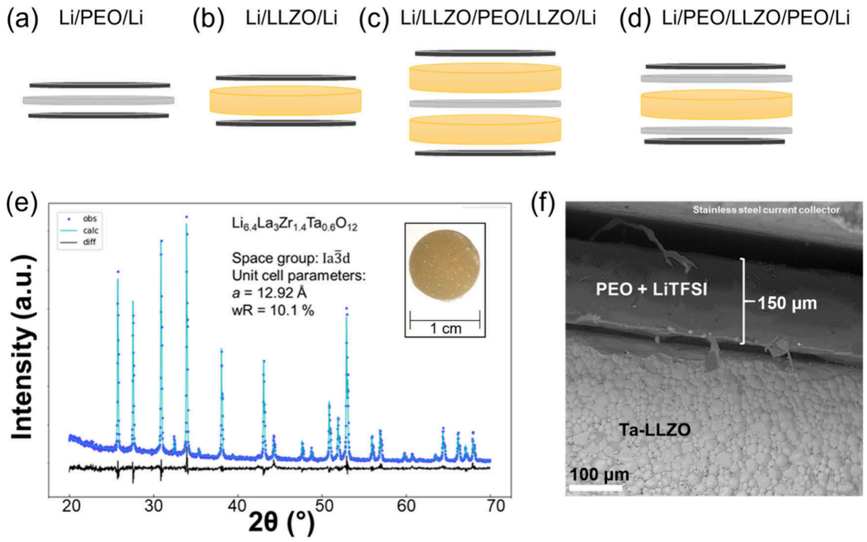

Figure 1. Top: Complementary solid-state symmetric cells used to investigate interfacial kinetics: (a) Li/PEO/Li cell, (b) Li/LLZO/Li cell, (c) Li/LLZO/PEO/LLZO/Li cell, (d) Li/PEO/LLZO/PEO/Li cell. (e) Rietveld refinement of powder X-ray diffraction data of the as-synthesized LLZO, indicating that the material is highly crystalline and phase-pure. An image of an as-synthesized LLZO pellet is shown in the inset. (f) SEM image of a deconstructed Li/PEO/LLZO/PEO/Li cell showing the ~150 μm thickness of the as-prepared PEO electrolyte on top of the LLZO pellet.

have considerably lower ionic conductivity than current state-of-the-art liquid[22] and solid electrolytes[23] at room temperature, but also they have been shown to have large interfacial impedances against Li metal (kΩ·cm^2 at room temperature).[11,24,25] Composite electrolytes comprised of both ceramic and solid polymer electrolytes may enable solid-state batteries that benefit from the mechanical properties of polymers and high ionic conductivity and interfacial kinetics of ceramics. For example, blending LLZO (conductivity of 10^{-4}–10^{-3} S cm^{-1} at room temperature)[23] into PEO-based electrolytes (conductivity up to 10^{-4} S cm^{-1} at room temperature),[22,26] can result in composite electrolytes that are more conductive than PEO, and yet mechanically flexible enough to maintain good interfacial contact with the electrodes.[19,27,28]

Directly probing charge transfer resistances at interfaces between electrolytes (ceramic/polymer interfaces) and lithium (lithium/ceramic and lithium/polymer interfaces) is nontrivial in composite electrolytes. First, the interfacial impedance of Li/LLZO is highly dependent on the interfacial chemistry, where exposure to different solvents or salts commonly used in liquid or polymer electrolytes,[29] as well as exposure to air,[30−32] leads to the formation of surface contaminants that drastically lower the effective conductivity of LLZO. Second, the contact area of polymer or ceramic electrolytes with lithium is not well-defined in conventional composite electrolytes, which can be solved by using multilayer electrolyte architectures that combine solid polymer and ceramic electrolytes in distinct layers.[33−35] Through electrochemical impedance spectroscopy (EIS) of symmetric cells featuring polymer/LLZO or polymer/$Li_{(1+x)}Al_xTi_{(2-x)}(PO_4)_3$ (LATP) multilayer electrolytes, Trevisanello et al.[36] have reported room-temperature interfacial resistances on the order of kΩ·cm^2, consistent with the findings of Isaac et al.[37] that show kΩ·cm^2 resistances at the PEO/LATP interface. While these studies of multilayer cells shed light on the magnitude of interfacial impedance by using EIS, they provide limited information on the mechanisms of interfacial processes, as they do not specifically isolate different sources of interfacial impedance in these systems. Given that rate capabilities and cell overpotentials are often dominated by interfacial electrochemical processes in solid-state batteries,[3] a deeper fundamental understanding of the electrochemical kinetics of ion transport near interfaces and charge transfer across interfaces is crucial in order to optimize the performance of composite and multilayer solid-state batteries.

In this work, we employ EIS and cyclic voltammetry to rigorously quantify charge transfer resistances, exchange current densities, and interfacial film resistances at Li/PEO, Li/LLZO, and PEO/LLZO interfaces (Note: herein, 'charge transfer' is used as a general term encompassing the transfer of ions and/or electrons across an interface. For instances in which it is possible to describe a charge transfer reaction in terms of its specific ionic or electronic contributions, we will further break down analysis of 'charge transfer' reactions into explicit discussions of interfacial 'ion transfer' or 'electron transfer'). Cell architectures are systematically varied (Figure 1a) to isolate and compare ion transport in both PEO and LLZO electrolytes as well as the charge transfer kinetics at Li/PEO interfaces, Li/LLZO interfaces, and PEO/LLZO interfaces. By complementing interfacial impedance analysis with the fitting of electrochemical models of charge transfer kinetics to experimental DC polarization data that extends beyond the potential window of typical EIS measurements, interfacial charge transfer impedances are decoupled from ion transport impedances that appear in a similar frequency region and arise from poorly conductive surface films. Notably, charge transfer at the Li/PEO interface is limited by the rate of ion transfer (rather than electron transfer). Additionally, it is observed that the charge transfer resistance at the Li/LLZO interface is not limiting in the studied cell architectures, which is then leveraged to investigate ion transfer kinetics at PEO/LLZO interfaces using Li/LLZO/PEO/LLZO/Li cells. It is found that slow charge transfer and large impedances of the PEO/LLZO interface are due to contaminants on the LLZO surface, the latter of which can be decreased by heat-treating LLZO prior to battery assembly. Therefore, controlling for chemistry at polymer/ceramic interfaces is essential to reduce ion transport limitations through interfacial contamination layers. Our findings provide new insights into the charge transfer limiting steps and sources of overpotential at interfaces in multilayer and composite solid electrolytes.

EXPERIMENTAL SECTION

LLZO Solid-State Synthesis. $Li_{6.4}La_3Zr_{1.4}Ta_{0.6}O_{12}$ was synthesized in a manner similar to previous reports.[38] All precursors were purchased from Sigma-Aldrich. ZrO_2, Ta_2O_5, La_2O_3, and Li_2CO_3 were mixed according to the stoichiometric ratios of the metals by grinding together with a mortar and pestle. A 10% stoichiometric excess Li_2CO_3 was used to account for lithium evaporation during synthesis. These materials were placed in a MgO crucible and calcined at 900 °C for 6 h under flow of oxygen. A ramp rate of 3 °C/min was used for both heating and cooling. Following calcination, the calcined powder was ground again. A portion of this calcined powder was then mixed with polyvinyl butyral binder (PVB) in isopropanol to make a mixture that was 5% PVB by weight. This mixture was then allowed to dry under ambient conditions, before 400 mg quantities of the powder were placed in a 1 cm diameter pellet die and pressed at 5 t of pressure for 2 min. The resulting pellets were then placed on a bed of the calcined powder (not containing PVB) and then covered with a small amount of calcined powder in a MgO crucible. The pellets were then sintered at 1230 °C for 6 h under a flow of oxygen. The resulting LLZO pellets (∼1 mm thickness, ∼1 cm diameter) were polished to a mirror finish (Figure 1e) using sandpaper and colloidal diamond polishing fluids on an AutoMet Buehler polishing machine. Before use in batteries, polished LLZO pellets were heat treated at either 500 or 700 °C (as specified in the main text) for 3 h in an argon glovebox using a muffle furnace.

PEO Electrolyte Preparation. Polymer electrolyte films were prepared by mixing poly(ethylene oxide) powder (MW = 600 K, Sigma-Aldrich) with lithium bis(trifluoromethanesulfonyl)imide (LiTFSI, Sigma-Aldrich) in a 17.5:1 EO:Li ratio (1.28 molal, 1 molar) in an argon-filled glovebox. This mixture was then dissolved in acetonitrile to make a 2% by weight solution of PEO. Three × 100 μL aliquots of the solution were then drop cast onto 1 cm diameter Teflon substrates, allowing the acetonitrile to evaporate between each aliquot. The resulting films were then dried under vacuum at 80 °C for ∼6 h.

Battery Assembly. All cells were assembled in an argon-filled glovebox (O_2, $H_2O < 0.1$ ppm) in Swagelok T-cells using stainless steel dies as current collectors. Lithium foils (MTI, 6 mm diameter, 150 μm thickness) were polished in the glovebox using a steel spatula to remove the native oxide surface layers. Such treatment yielded foils with a mirror-like finish that could then be used in battery cells, built as described in the following: *Li/PEO/Li and SS/PEO/SS Cells:* PEO-containing cells were built by placing ∼150 μm thick PEO electrolytes on top of 100 μm-thick PTFE spacers. This assembly was then inserted between the desired electrodes, with either Li foils or stainless-steel current collectors placed above and below the assembly. Following assembly, the cells were heat treated at 80 °C for 3 h in a muffle furnace inside the glovebox, and then cooled to room temperature before further testing. This step helped accelerate the formation of a stable passivation layer at the Li/PEO interface. Notably, the film resistance at the Li/PEO interface is highly dependent on the thermal and cycling history of the cells. For example, when assembling cells without the 80 °C treatment, we found that the Li/PEO interfacial impedance grew slowly (but substantially) over time (Figure S1). The variation in interfacial film resistance with the treatment method can be attributed to a different SEI thickness and chemistry as well as different wetting of the lithium metal electrode.[39,40] *Li/LLZO/Li Cells:* In order to achieve low impedance at the Li/LLZO interface, contaminants such as Li_2CO_3 and LiOH must be removed from the surface of LLZO.[30,31,41] We followed a procedure as developed by Sharafi et al., whereby LLZO pellets were heat treated at 500 °C for 3 h in a muffle furnace in the glovebox (ramp rate of 5 °C min^{-1}).[30] After 3 h at temperature, the pellets were removed while the furnace was still hot (300−400 °C) and they were used *immediately* for the construction of Li/LLZO/Li symmetric cells. The cells were placed in the Swagelok T-cell with a stiff spring and a hand press was used to apply ∼250 kPa of stack pressure. The cells were then transferred to a muffle furnace in the glovebox and heated at 175 °C for 3 h. Cells were then allowed to cool to room temperature before further testing. *Li/LLZO/PEO/LLZO/Li Cells:* Assembling Li/LLZO/PEO/LLZO/Li cells is a two-step process: First, two LLZO pellets are heat treated at 500 °C as described above for Li/LLZO/Li cells. Then, a lithium foil is applied to one face of each pellet, and heat treated at 175 °C as above to make a low-impedance Li/LLZO interface. Second, a PEO film is inserted between the open faces of the LLZO pellets, placed in a Swagelok cell, and heat treated at 80 °C for 3 h in the glovebox. Cells were then allowed to cool to room temperature before further testing. *Li/PEO/LLZO/PEO/Li Cells:* LLZO pellets were first heat treated 500 °C as described above. Polymer films were then placed on either side of the LLZO pellet, followed by 6 mm Li foils. Cells were then heat treated at 80 °C for 3 h in the glovebox, and then allowed to cool to room temperature before further testing. To optimize and further reduce the impedance of the PEO/LLZO interface, additional cells of this type were built by increasing the LLZO bake temperature to 700 °C, leaving all other processing conditions constant.

Electrochemical Testing. All electrochemical tests of the cell types described above were performed on a Biologic SP-300 potentiostat. Variable temperature measurements were carried out from 30−80 °C by stepwise heating in 10 °C increments using an SU-241 Espec Temperature Chamber. Cells were allowed to equilibrate at each temperature for 30 min prior to any testing. Data presented in figures in the main text focus on data collected at 60 °C and above, where PEO is molten and amorphous.[36] EIS measurements were carried out using a frequency range of 7 MHz−1 Hz with a voltage amplitude of ±10 mV. All EIS parameter values reported in tables herein refer to full-cell values; for per-interface values of charge transfer resistance, film resistance, etc., the values can be divided by two. All CVs are reported with voltage as the raw voltage of the working electrode divided by two in order to yield the overpotential of the working electrode vs Li^+/Li. All Tafel plots of CV data were *iR* corrected by accounting for the voltage drop associated with bulk and grain boundary conductivity. Arrhenius plots of exchange current density consider the per-interface values, rather than full-cell values. Conductivity was calculated using the formula $\sigma = l/(R*A)$, where l is the electrolyte thickness, A is the area of the electrode, and R is the total electrolyte resistance measured by EIS. Cyclic voltammetry (CV) was performed using a scan rate of 100 mV s^{-1}. It was found that slower scan rates led to strong hysteresis in lithium stripping/plating at Li/LLZO interfaces (Figure S2), which likely arises due to non-negligible changes in electrolyte/electrode contact area during anodic dissolution of lithium.[6] Distribution of relaxation times (DRT) were calculated using the DRT.jl package in Julia,[42] with a regularization hyperparameter of 0.01. Charge transfer kinetics were analyzed within the frameworks of the Butler−Volmer model, as well as Marcus-based theories of electron transfer (for equations and fitting details, see SI).

Characterization. ^1H, ^7Li, ^{13}C, and ^{19}F solid-state nuclear magnetic resonance (NMR) spectra of composite PEO+LLZO electrolytes were collected on a Bruker Avance Neo 500 MHz spectrometer with magic angle spinning at 20 kHz. Composite samples were prepared in a solvent-free manner by crushing heat-treated LLZO into powder, and then grinding the resulting powder with a PEO polymer electrolyte film in a mortar and pestle in an argon-filled glovebox. Powder X-ray diffraction patterns were measured using a Bruker D2 Phaser. Rietveld refinements of the powder diffraction data was performed against the published crystal structure of Ta-doped LLZO (space group 1a$\bar{3}$d), yielding a refined lattice parameter of $a = 12.92$ Å (Figure 1e), in good agreement with previous reports.[43] To image cross sections of the multilayer electrolytes, samples were prepared in a glovebox, then transferred to a Leica VCM liquid-nitrogen-filled sample prep station. Samples were immersed and fractured in liquid nitrogen, then transferred in a Leica VCT500 air-free transfer shuttle to the Zeiss Crossbeam 540 SEM equipped with a Leica cryostage. SEM imaging was performed on a Zeiss Crossbeam 540 SEM using an accelerating voltage of 2 kV and a probe current of 100 pA. X-ray photoelectron spectroscopy (XPS) was carried out on a PHI VersaProbe II X-ray Photoelectron Spectrometer with a monochromated Al K-alpha X-ray source. Given that LLZO is insulating, all spectra were recorded with use of a neutralizer. Heat-treated LLZO samples were transferred from the glovebox into the XPS instrument via a portable transfer vessel that enables sample introduction without exposure to air. XPS data were analyzed using CasaXPS[44] and relative sensitivity factors specific to the PHI VersaProbe II X-ray Photoelectron Spectrometer. All samples were referenced to the adventitious C 1s peak at 284.8 eV.

RESULTS AND DISCUSSION

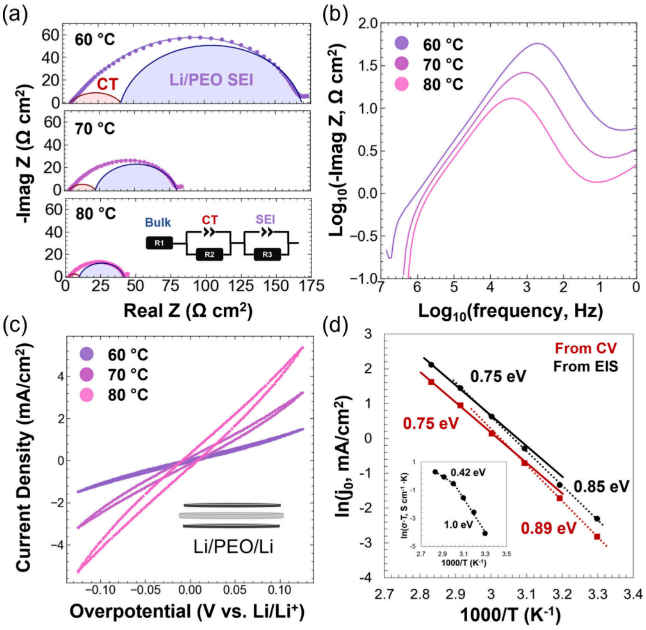

Figure 2. (a) Nyquist plots of a symmetric Li/PEO/Li cell from 60 to 80 °C and the corresponding equivalent circuit used to fit the spectra. The total fits are included as solid lines through the data points, and contributions from individual RC circuit elements are shown in the shaded areas (shaded red = charge transfer, purple = SEI). EIS fitting parameters can be found in Tables 1, S1. (b) Bode plots of the raw data shown in panel (a). (c) Representative cyclic voltammograms of a Li/PEO/Li cell from 60 to 80 °C. (d) Arrhenius plots of the per-interface exchange current density j_0 at the Li/PEO interface, as determined by EIS (black) and CV measurements (red). The temperature dependence of the ionic conductivity of the PEO is shown in the inset.

Table 1. Equivalent Circuit Values Corresponding to the Fit of the Nyquist Plot of the Li/PEO/Li Cell at 80 °C Shown in Figure 2a[a]

Circuit element	Value	Units	RC time constant τ (s)	Assignment
R1	2.6	Ω cm^2	-	Bulk electrolyte resistance of PEO
R2 (resistance)	31.7	Ω cm^2	7.1×10^{-5}	SEI of two Li/PEO interfaces
Q2 (capacitance)	1.3×10^{-5}	F/cm^2		
α2 (CPE exponent)	0.82	-		
R3	7.4	Ω cm^2	1.1×10^{-5}	Charge transfer at two Li/SEI/PEO interfaces
Q3	8.1×10^{-5}	F/cm^2		
α3	0.65	-		

[a] Time constants of different processes were calculated through $\tau = (QR)^{1/\alpha}$.

Li/PEO Interface. To begin investigations of the charge transfer kinetics at the Li/PEO interface, EIS analysis was carried out on symmetric Li/PEO/Li cells (Figure 1a). The dominant source of impedance is the midfrequency feature, which appears in the EIS of the Li/PEO/Li cell as an elongated semicircle in the Nyquist plot (Figure 2a), spanning frequencies from ~10^2 Hz to ~10^4 Hz from 60 to 80 °C in the Bode plots (Figure 2b). This is in line with previous studies that have characterized Li/PEO interfaces, reporting similar values of impedance[11,25,39,40,45,46] and attributing the origin of the high interfacial impedance for PEO electrolytes with LiTFSI salt to organic and inorganic decomposition products (the solid electrolyte interphase, SEI), arising from reactions between PEO and the TFSI anion with lithium metal at the interface.[47−49] Thus, sources of impedance in the midfrequency window of Figure 2a,b include (1) ion transport through the SEI and (2) ion and electron transfer reactions at the Li/PEO interface. Unambiguous deconvolution of the impedance associated with ion transport through the SEI and with charge transfer reactions at the Li/PEO interface is nontrivial using solely EIS, as these processes overlap in the same frequency window.[50] The impedance associated with bulk ion transport in the PEO electrolyte is not visible in the spectra in Figure 2a,b, as from 60 to 80 °C the bulk conductivity response exceeds the potentiostat frequency limit of 7 MHz. Therefore, at 80 °C, the ionic conductivity of 1 M LiTFSI in the PEO electrolyte (3.8 mS cm^{-1}, in agreement with previous reports[19,37]) is captured as an electrolyte resistance term in the EIS fitting (R1 in Table 1), rather than as an RC circuit element. At lower temperatures (30 to 40 °C), bulk ion transport appears as distinct semicircle in the Nyquist plot (Figure S3a, Table S1) at frequencies between 10^6 and 10^7 Hz (Bode plot in Figure S3c). To confirm that this high-frequency semicircle corresponds to ion transport in bulk PEO, we isolate the bulk conductivity response by EIS of PEO with stainless steel blocking electrodes (Figure S4, Table S2). Across the entire investigated temperature range, it is clear that the main source of impedance in Li/PEO/Li comes from the Li/PEO interface, rather than from bulk ion transport.

To further understand the contributions to the interfacial impedance and limiting steps of charge transfer at the Li/PEO interface, we measure the DC polarization response of the symmetric Li/PEO/Li cells from 30−80 °C (Figure 2c, Figure S3d-f) and use electrochemical kinetic models to extract the SEI ohmic resistance and the exchange current density according to Butler−Volmer-based kinetics. More specifically, in order to deconvolute the resistance associated with ion transport through the SEI film from the charge transfer resistance, equations of electrode kinetics need to include a term to capture the iR drop associated with the SEI film resistance. This can be achieved by fitting experimental DC polarization curves to a modified Butler−Volmer equation as shown in eq 1, where j is the total current, j_0 is the exchange current density, α is the charge transfer coefficient, z is the number of electrons participating in the electrode reaction, F is Faraday's constant, R is the ideal gas constant, T is the temperature, η_{total} is the total electrode surface overpotential, and R_{film} is the SEI film resistance:

$$j = j_0\left(\exp\left(-\frac{\alpha zF}{RT}(\eta_{total} - jR_{film})\right) - \exp\left(\frac{(1-\alpha)zF}{RT}(\eta_{total} - jR_{film})\right)\right) \tag{1}$$

In eq 1, the voltage drop from the SEI film resistance term is subtracted from the total surface overpotential, leaving behind the fraction of the surface overpotential associated with driving the charge transfer reaction. Treating R_{film} as a fitting parameter

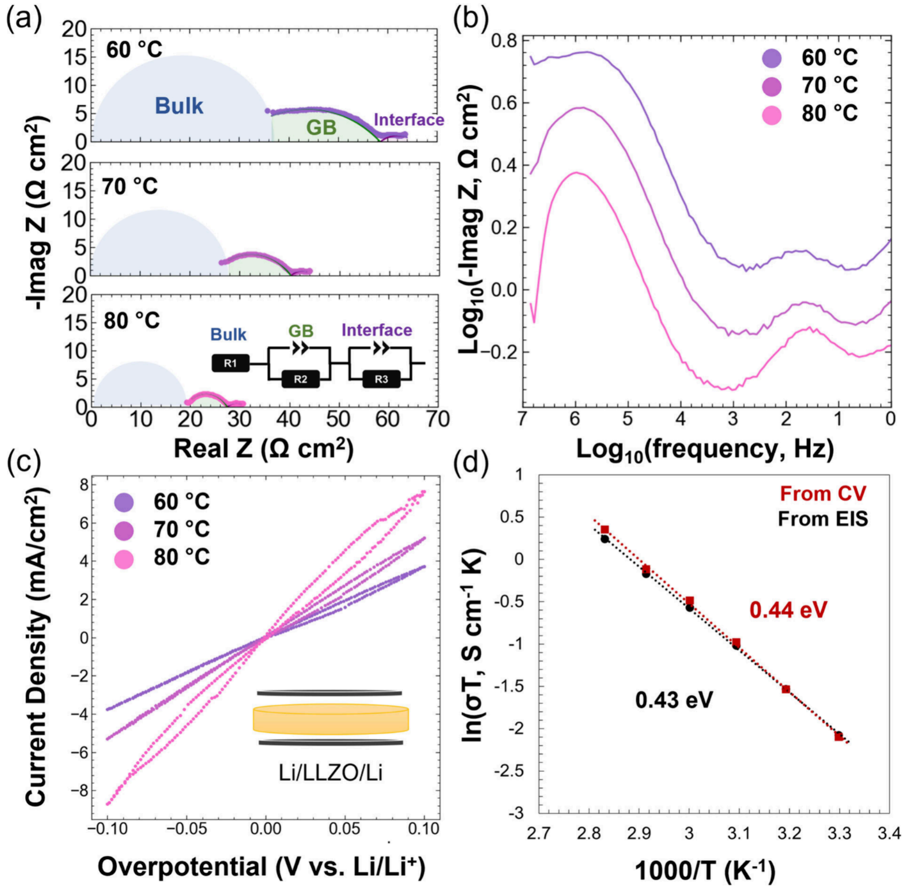

Figure 3. (a) Nyquist plots of a symmetric Li/LLZO/Li cell from 60 to 80 °C and the corresponding equivalent circuits used to fit the spectra. The total fits are included as solid lines through the data points, and contributions from individual RC circuit elements are shown in the shaded areas (shaded blue = bulk ionic conductivity, green = grain boundary conductivity, purple = total interfacial impedance). EIS fitting parameters can be found in Table 2 and Table S5. (b) Bode plots of the raw data shown in panel (a). (c) Representative cyclic voltammograms of the Li/LLZO/Li cell from 60 to 80 °C. (d) Arrhenius plots of the total conductivity σ (bulk and grain) as determined by EIS (black) and CV measurements (red).

in a modified form of eq 1 (see Equation S5 and details on the electrochemical models and fitting in the Supporting Information) thus enables more accurate assessments of the exchange current density and charge transfer resistance.

With the inclusion of a film resistance term into the Butler−Volmer-based model (eqs 1, S4, and S5),[51,52] it was possible to fit the current−voltage responses in a limited voltage window (from −0.125 to 0.125 V vs Li$^+$/Li) across the 30 to 80 °C temperature range (Figure S 3d-f). While applying higher overpotentials consistently shorted cells at high temperatures, the model was also tested in a wider window of overpotentials (from −0.25 to 0.25 V vs Li$^+$/Li) on data acquired at 30 °C in Figure S5, where the CV is clearly nonlinear and charge transfer reactions at the Li/PEO interface are likely rate-limiting. The SEI resistance obtained from the fitting of a film resistance parameter in our Butler−Volmer analysis of the CV at 30 °C is on the order of 2300−2400 Ω cm^2 (Figure S7), similar in magnitude to the largest contribution to the interfacial resistance as determined by EIS equivalent circuit fitting (∼2700 Ω cm^2, Figure S3a and R5 in Table S1). Therefore, this larger impedance contribution can be attributed to slow ion transport in the SEI, indicating that the smaller impedance contribution in this frequency region (∼260 Ω cm^2, R4 in Table S1) can be assigned to the charge transfer resistance at the Li/PEO interface. Thus, by matching the film resistance of the SEI as determined by fitting of DC polarization data in the nonlinear response regime, we were able to deconvolute charge transfer impedance from SEI ion transport impedance, enabling the unambiguous assignment of the RC circuit elements in equivalent circuit modeling of EIS data across the entire temperature window (Figure 2a, Figure S3a,b).

By complementing EIS analysis with the fitting of the CV data, the deconvolution of the SEI resistances from the charge transfer resistances leads to a good agreement between the exchange current densities determined by CV and EIS across the entire 30−80 °C temperature range (Figure 2d). Indeed, the exchange current density from the modified Butler−Volmer model (5.0 mA/cm^2 at 80 °C) was found to differ by only a factor of 1.6 from the exchange current density measured from EIS measurements (8.3 mA/cm^2 at 80 °C, calculated from the charge transfer resistance from EIS, R3 in Table 1). This agreement is encouraging, as it is has been shown that reported values of exchange current density often differ by an order of magnitude or more between distinct methods of measurement.[10,36] By including a film resistance term into the Butler−Volmer equation, the model provided a close fit to the nonlinear response of the Li/PEO interface across a wide range of overpotentials (Figure S5, Figure S8). Without the film resistance term, the standard Butler−Volmer equation could only provide a satisfactory fit and accurate estimation of j_0 within the narrow window of overpotentials in which the CV behaves linearly (± 25 mV), Figure S8.

The activation energy of the exchange current density at the Li/PEO interface was found to be 0.75 eV between 60 and 80 °C (Figure 2d), which agrees with the reported interfacial activation energies at Li/PEO interfaces.[36,39,40] This value is markedly different from the activation energy of the bulk conductivity of PEO (0.42 eV) measured by EIS across the same temperature range (Figure 2d inset), in agreement with previous work.[19,37] Decreasing temperatures to the range between 30 and 50 °C, where PEO exists in both amorphous and crystalline domains,[53] the activation energy was found to be 0.85−0.89 eV as determined by EIS or CV, respectively (Figure 2d), which corroborates the findings of Trevisanello et al.[36] that PEO crystallization has an influence on the activation energy of the interfacial impedance. Interestingly, these experimentally measured values of the activation energy hint at which charge transfer step (ion or electron transfer) is rate-limiting at the Li/PEO interface. Indeed, if we fit Li/PEO polarization curves with Marcus-based models that assume electron transfer (rather than ion transfer) is rate-limiting to the charge transfer kinetics, we found that such models vastly underpredicted the activation energy of charge transfer, yielding activation energies of 35−60 mV, which are more than an order of magnitude smaller than the experimentally measured activation energies shown in Figure 2d (see Note S2 and Figure S8 for more discussion and analysis regarding Marcus-based kinetics). Therefore, the charge transfer kinetics at the Li/PEO interface are likely limited by the rate of ion transfer, rather than electron transfer under these conditions.

Li/LLZO Interface. In contrast to the Li/PEO/Li cells, bulk and grain boundary conductivity are the largest sources of impedance in Li/LLZO/Li cells, where the total conductivity considering both bulk and grain boundary resistance was found to be σ_{total} = 3.6 mS cm^{-1} at 80 °C, in accordance with previous reports.[36,54] At 30 °C, the measured bulk conductivity response of LLZO extracted from the data in Figure S9a is 0.7 mS cm^{-1} and its impedance has a characteristic frequency of ∼7 MHz (Figure S9), which also matches previously reported values and characteristic frequencies of bulk ionic conductivity in LLZO.[30] At higher temperatures (60 to 80 °C), the impedance associated with bulk conductivity shifts to frequencies above 7 MHz and is not seen in the Nyquist plots in Figure 3a. The impedance response observed in the 10^5−10^6 Hz frequency range (Figure 3b) corresponds to grain boundary conductivity with a characteristic frequency of 100 kHz at 80 °C, as determined by the peak in the Bode plot. This assignment is supported by the work of Dudney et al.[55] in which it was found that LLZO grain boundary conduction has characteristic frequencies in the hundreds of kHz regime at elevated temperatures.

Sources of impedance from the Li/LLZO interface are small and at 30 °C; the impedance contribution of the Li/LLZO interface is nearly negligible and is difficult to evaluate as only a short tail arising from interfacial impedance can be measured at this temperature (Figure S9a). Here, more than 90% of the total resistance of the cell comes from bulk and grain boundary contributions (Table S5). At higher temperatures, the interface signal appears in the Nyquist plot in Figure 3a at frequencies from 10^1 Hz to 10^3 Hz (Figure 3b), and the total interfacial impedance at 80 °C is 3.6 Ω cm^2 (Table 2, Figure 3a). Here, it is important to note that the total interfacial impedance consists of contributions arising from a combination of charge transfer resistance,[6,17] constriction effects due to imperfect contact with the Li metal anodes,[9,17] residual contamination layers at the interface,[30] and diffusion effects,[9,31,56] where these latter contributions contribute much more than charge transfer resistance.[6,17] Considering the varied sources of interfacial impedance at the Li/LLZO interface, it is noteworthy that the impedance associated with bulk and grain boundary ion transport in LLZO still dominates at elevated temperatures (about 27.5 Ω cm^2 at 80 °C in Figure 3a, Table 2). Indeed, due to the rapid rates of interfacial charge transfer,[55] the kinetics in Li/LLZO systems are characterized by mass transport-limited behavior where the migration of ions through the bulk of the electrolyte is rate-determining and the corresponding DC polarization responses are linear within the limit of electrolyte stability and in the absence of lithium dendrite formation.[3,6,9,13] Measuring the CVs of symmetric Li/LLZO/Li cells from 30 to 80 °C (Figure 3c, Figure S10d,e) results in linear CVs that only show deviations from linearity at high current densities at 80 °C due to lithium dendrite penetration of the LLZO pellet that caused the cell to short circuit in subsequent CV cycles. The temperature dependence of the total conductivity of LLZO as determined by EIS (Figure 3d) displays Arrhenius behavior with an activation energy of 0.43 eV (Figure 3d, black data points), which is in close agreement with reported activation energy values for ion transport in LLZO (∼0.40 eV).[55,9,57] If ion transport in LLZO is indeed the dominant factor in the electrochemical kinetics of this system, then the total conductivity of LLZO can also be found from the CV data, as it should be proportional to the reciprocal of the slope of the data shown in Figure 3c and Figure S10e. Plotting conductivity as determined by CV yields a close match to the results from EIS (Figure 3d, red data points, E_A = 0.44 eV). These findings support that ion transport governs the kinetics for Li/LLZO/Li cells, and the charge transfer resistance at the Li/LLZO interface is not limiting. We next use the fact that the Li/LLZO interface has small impedance and non-rate-limiting charge transfer kinetics to isolate the effects of PEO/LLZO interfaces in Li/LLZO/PEO/LLZO/Li cells.

Table 2. Equivalent Circuit Values Corresponding to the Fit of the Nyquist Plot of the Li/LLZO/Li Symmetric Cell at 80 °C Shown in Figure 3a[a]

Circuit element	Value	Units	RC time constant τ (s)	Assignment
R1	19.0	Ω cm^2	-	Bulk electrolyte resistance
R2 (resistance)	8.5	Ω cm^2	2.1 × 10^{-7}	Grain boundary electrolyte resistance
Q2 (capacitance)	5.3 × 10^{-6}	F/cm^2		
$\alpha 2$ (CPE exponent)	0.65	-		
R3	3.6	Ω cm^2	4.8 × 10^{-3}	Interfacial impedance of 2 Li/LLZO Interfaces
Q3	1.9 × 10^{-3}	F/cm^2		
$\alpha 3$	0.46	-		

[a] Time constants of different processes were calculated through $\tau = (QR)^{1/\alpha}$.

PEO/LLZO Interface. Since the impedance of the Li/LLZO interface is negligible in the presence of much larger sources of impedance, we can isolate the effects of PEO/LLZO interfaces by assembling Li/LLZO/PEO/LLZO/Li cells as shown in Figure 1c. This cell configuration is advantageous in that it enables an investigation of ion transfer kinetics at the PEO/

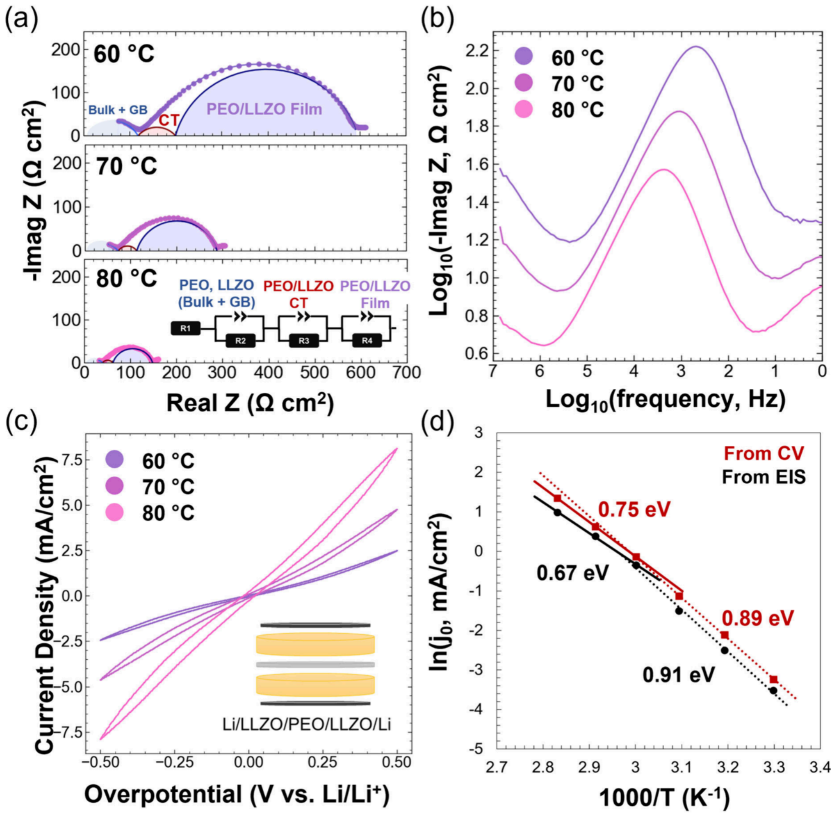

Figure 4. (a) Nyquist plots of a symmetric Li/LLZO/PEO/LLZO/Li from 60 to 80 °C and the corresponding equivalent circuits used to fit the spectra. The total fits are included as solid lines through the data points, and contributions from individual RC circuit elements are shown in the shaded areas (shaded blue = bulk and grain boundary impedance, red = charge transfer at the PEO/LLZO interface, purple = film resistance from contamination layers at the PEO/LLZO interface). EIS fitting parameters can be found in Tables 3, S6. (b) Bode plots of the raw data shown in panel (a). (c) Representative cyclic voltammograms of the symmetric Li/LLZO/PEO/LLZO/Li cell from 60 to 80 °C. (d) Arrhenius plots of the per-interface exchange current density j_0 of ion transfer across the PEO/LLZO interface as determined by EIS (black) and CV measurements (red).

LLZO interface in the absence of a significant response from the electrolyte interface with the lithium electrode and without the use of blocking electrodes that would otherwise interfere with the EIS response at low frequencies or with DC polarization measurements. Similar to the impedance analyses of Li/PEO/Li and Li/LLZO/Li cells, the Nyquist and Bode plots of a Li/LLZO/PEO/LLZO/Li cell display high frequency features ($>10^6$ Hz in Figure 4b, Figure S12) that comprise the conductivities of both LiTFSI in PEO as well as the bulk and grain conductivities of the LLZO. In contrast to the Li/LLZO/Li cell, it is apparent from the Nyquist and Bode plots of the Li/LLZO/PEO/LLZO/Li cell between 60−80 °C (Figure 4a,b) that the impedance response is dominated by processes that occur in the midfrequency region (10^2−10^4 Hz). Since the Li/LLZO interface contributes very little total impedance, particularly within this frequency region, this response must arise from the PEO/LLZO interface.

DC polarization curves for Li/LLZO/PEO/LLZO/Li cells are nonlinear (Figure 4c, Figures S11, S12), a feature that must originate *purely from ion transfer* across the PEO/LLZO interface, as the charge transfer kinetics at the Li/LLZO interface are not rate-limiting and cannot account for this curvature. This is, to our knowledge, the first time that the nonlinear behavior of ion transfer across a ceramic/polymer electrolyte interface has been clearly demonstrated through DC polarization experiments. The nonlinear nature of the ion transfer kinetics at the PEO/LLZO interface is best visualized at lower temperatures (30 °C, Figure S11a), where the exchange current density is low enough to prevent the response from linearizing within the tested voltage window. Employing a Butler−Volmer model with a film resistance term yields close fits to the CV data (Figures S12, S13). The value of film resistance at 30 °C as determined by CV fitting (6000−6200 Ω cm^2) or EIS fitting (∼6760 Ω cm^2, Table S6) is larger than the charge transfer resistance associated with ion transfer (∼1770 Ω cm^2, Table S6). In this case, the large ‘film resistance’ at the PEO/LLZO interface likely originates from contamination layers that can spontaneously form on LLZO surfaces. Indeed, it has been suggested that LiOH layers can grow on the surface of the LLZO when placed in contact with PEO-based electrolytes,[36] and LiOH and Li_2CO_3 have been shown to form on LLZO in a matter of minutes even in a glovebox atmosphere.[31] The determination of the film resistance at the PEO/LLZO interface via fitting of CV data enabled unambiguous assignments of the EIS equivalent circuit elements across the entire temperature range (Figure 4a, Figure S12a,b), allowing for the identification of the distinct impedance contributions arising from ion transfer across the PEO/LLZO interface and ion transport through the interfacial contamination film.

The values of exchange current density for ion transfer at the PEO/LLZO interface as determined from CV (3.8 mA/cm^2 at 80 °C) are quite close to those that were determined from EIS fitting (2.6 mA/cm^2 at 80 °C, Figure 4d, Table 3). Between 60 and 80 °C, the activation energy of the exchange current density was found to be 0.67 eV by EIS and 0.75 eV by CV, respectively. Below the PEO melting point, the activation energies were

Table 3. Equivalent Circuit Values Corresponding to the Fit of the Nyquist Plot of the Symmetric Li/LLZO/PEO/LLZO/Li Cell at 80 °C Shown in Figure 4a[a]

Circuit element	Value	Units	RC time constant τ (s)	Assignment
R1	21.0	Ω cm^2	-	Bulk electrolyte resistance
R2 (resistance)	17.9	Ω cm^2	1.5×10^{-8}	Grain boundary electrolyte resistance
Q2 (capacitance)	1.6×10^{-7}	F/cm^2		
α2 (CPE exponent)	0.71	-		
R3	86.0	Ω cm^2	7.3×10^{-5}	Film resistance (LLZO surface contamination) at two PEO/LLZO interfaces
Q3	4.2×10^{-6}	F/cm^2		
α3	0.83	-		
R4	23.2	Ω cm^2	1.0×10^{-5}	Ion transfer resistance across two LLZO/PEO interfaces
Q4	3.7×10^{-5}	F/cm^2		
α4	0.61	-		

[a] Time constants of different processes were calculated through $\tau = (QR)^{1/\alpha}$. The impedance from the two Li/LLZO interfaces can be neglected, as the measured total interfacial resistance of these interfaces at 80 °C (Table 2) is ~3 Ω cm^2, which is <3% of the total interfacial resistance in this cell.

found to be 0.91 eV (EIS) and 0.89 eV (CV) (Figure 4d). These fall within the ranges of temperature-dependent activation energies of interfacial impedance in other ceramic/polymer systems as reported by several different EIS studies: PEO/LATP (0.67−0.85 eV),[36,37] PEO/LLTO (lithium lanthanum titanium oxide) interfaces (1.0 eV),[58] and PEO/LLZO interfaces (0.7−1.0 eV).[36,59] Interestingly, our findings show that the magnitude of the measured exchange current densities for ion transfer at the PEO/LLZO interface, and the activation energies thereof, are nearly the same as those determined for the Li/PEO interface (Figure 2d). This is noteworthy, as both electron and ion transfer occur at the Li/PEO interface, and yet its kinetics resemble that of the PEO/LLZO interface at which charge transfer reactions are purely ionic in nature. Indeed, the Bode plot of the Li/LLZO/PEO/LLZO/Li cell (Figure 4b) is quite similar to that of the Li/PEO/Li cell (Figure 2b), where maxima of the imaginary impedance occur within the same frequency window (10^3−10^4 Hz between 60−80 °C) for both cells. Moreover, the distribution of relaxation times for Li/PEO cells (Figure S6) resemble those of Li/LLZO/PEO/LLZO/Li cells (Figure S11b) and indicate that charge transfer occurs on a similar time scale at both PEO/LLZO interfaces and at Li/PEO interfaces. This congruence of the charge transfer kinetics of Li/PEO and PEO/LLZO interfaces provides further support that the charge transfer kinetics at these interfaces are limited by the rate of ion transfer, characterized by the (de)solvation of Li$^+$ ions in PEO.

Li/PEO/LLZO/PEO/Li Cells. Li/PEO/LLZO/PEO/Li cells (Figure 1d) represent the most practical architecture for multilayer solid electrolytes, where the polymer layers can provide improved contact at electrolyte/electrode interfaces. Figures S15, S16 illustrate the Nyquist plots of this cell type from

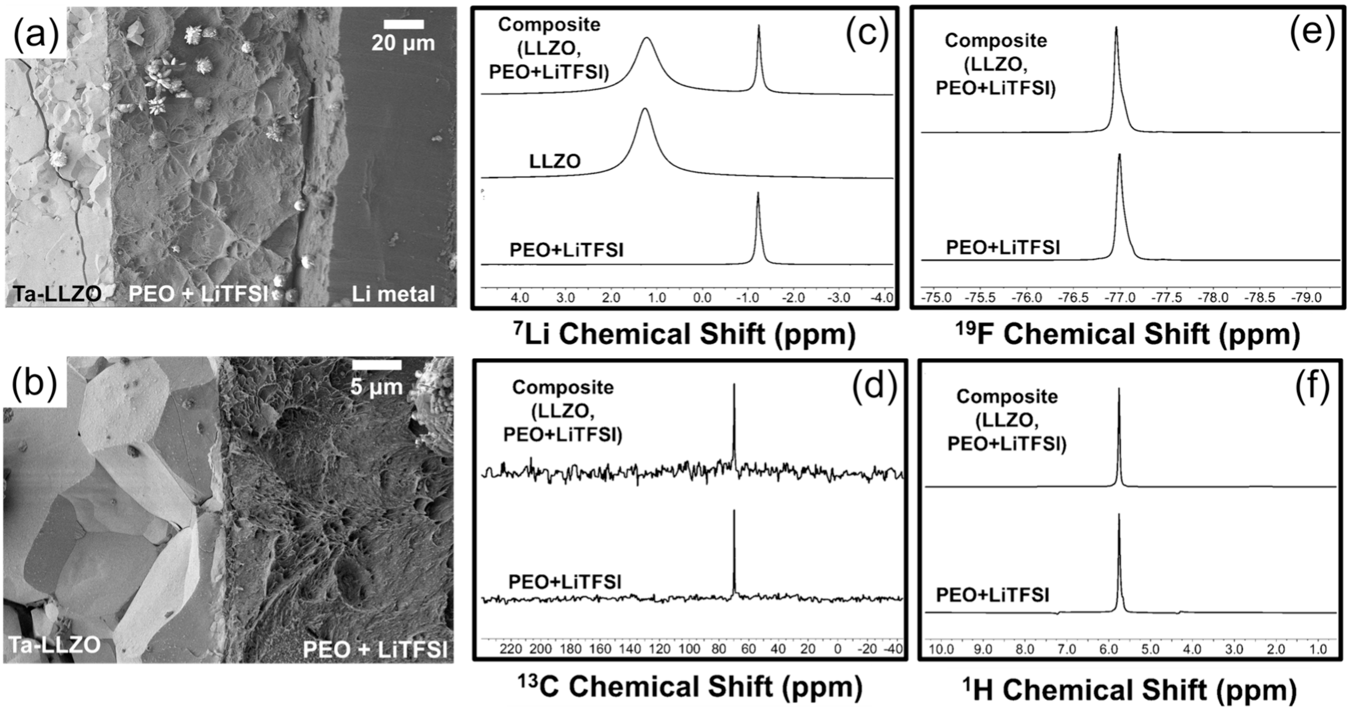

Figure 5. (a), (b) Cryo-SEM images of the cross section of a Li/PEO/LLZO/PEO/LLZO cell. Good contact is observed at LLZO/PEO and Li/PEO interfaces, and there is no indication of extensive chemical reactions occurring at either interface. The striations of the polymer are a result of the fracture process. Some ice crystal growths are observed on the surfaces of the PEO and LLZO, as sample transfer into the nitrogen-filled sample prep station required brief introduction of air into the sample chamber at liquid nitrogen temperatures. (c)-(f) Solid-state NMR spectra of a PEO/LLZO composite, pure LLZO, and pure PEO+LiTFSI. There is no indication of interfacial reactions in the composite as a result of contact between the LLZO and PEO+LiTFSI as the ^{7}Li, ^{19}F, ^{13}C, and ^{1}H NMR spectra of the composite show no new peaks or peak shifts as compared to the spectra of pure LLZO and pure PEO+LiTFSI.

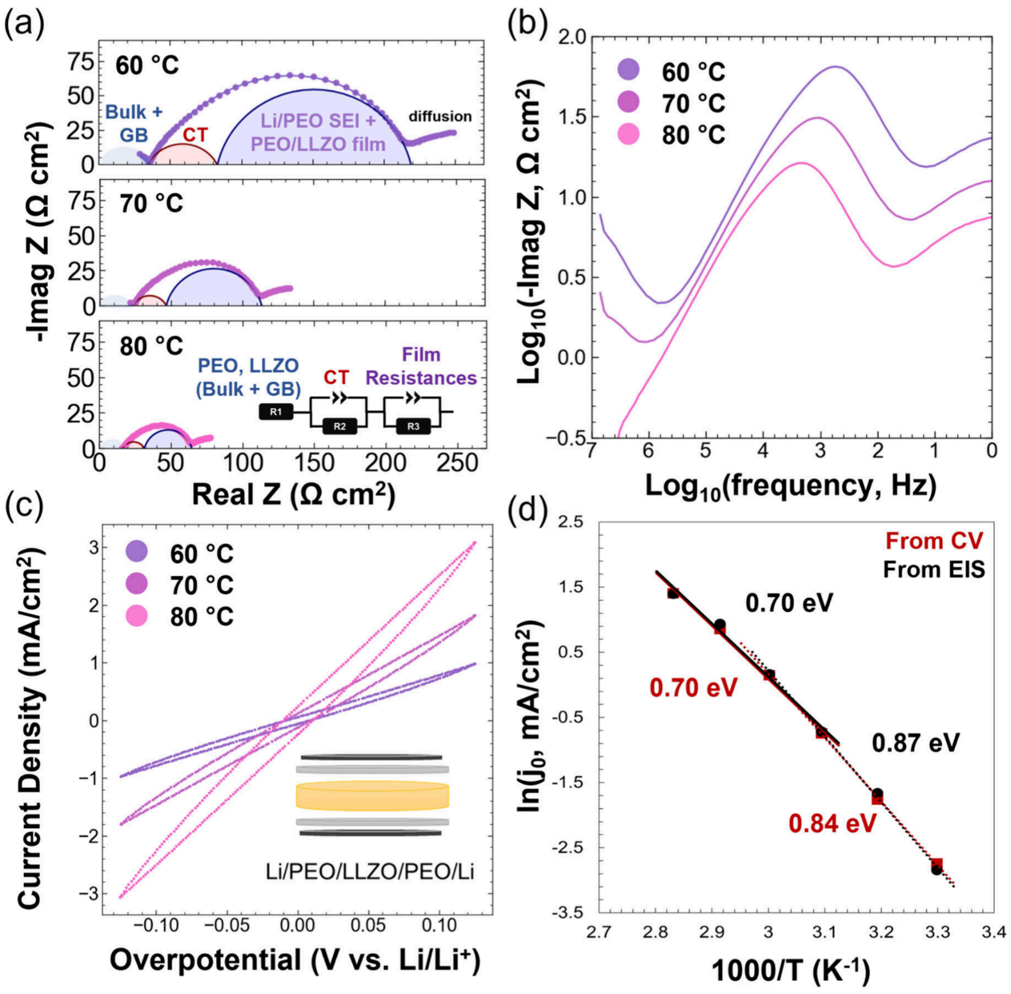

Figure 6. (a) Nyquist plots of a symmetric Li/PEO/LLZO/PEO/Li cell from 60 to 80 °C, and the corresponding equivalent circuits used to fit the spectra. The total fits are included as solid lines through the data points, and contributions from individual RC circuit elements are shown in the shaded areas (shaded blue = bulk and grain boundary impedance, red = combined charge transfer impedances from Li/PEO and PEO/LLZO interfaces, purple = combined impedance from contamination layers at PEO/LLZO interfaces and SEI from Li/PEO interfaces) (b) Bode plots of the raw data shown in panel (a). (c) Representative cyclic voltammograms of the symmetric Li/PEO/LLZO/PEO/Li cell from 60 to 80 °C. (d) Arrhenius plots of the exchange current density j_0 as determined by charge transfer resistances considering one PEO/LLZO and one Li/PEO interface as determined by EIS (black) and CV measurements (red).

30 to 80 °C. Comparing the total interfacial impedance of this cell at 30 °C (light blue trace, Figure S15a, ~7400 Ω cm^2) to that the interfacial impedance of a typical Li/PEO/Li cell at 30 °C (Figure S3a, ~2750 Ω cm^2, Table S1) reveals the large impedance contribution the PEO/LLZO interface imparts on this system (a difference of ~4650 Ω cm^2). As mentioned above, we found that a large source of impedance arises at the PEO/LLZO from contamination layers at the LLZO surface (Figure 4a, Table 3). While some reports have hypothesized that contamination layers form through reactions between PEO and LLZO,[36] solid-state NMR analysis of freshly prepared PEO/LLZO composites (Figure 5c-f) and SEM of cross sections of Li/PEO/LLZO/PEO/Li cells (Figure 5a,b) do not show any apparent evidence for a reaction at the PEO/LLZO interface, suggesting that the large interfacial impedance at the PEO/LLZO interface arises from residual contamination native to the LLZO surface even after a 500 °C heat treatment. Thus, we sought to reduce the interfacial resistance at the PEO/LLZO interface by optimizing the processing conditions for the removal of residual interfacial contamination layers on LLZO. Several recent studies have revealed the benefits of further increasing the temperature of the LLZO heat treatment in order to more completely remove these interfacial contaminants, with ~700 °C being close to the highest temperature that can be used without inducing formation of impurities in the LLZO through lithium loss.[60−62] Employing a 700 °C heat treatment to LLZO pellets yielded Li/PEO/LLZO/PEO/Li cells with an interfacial impedance that was 3600 Ω cm^2 lower as compared to the same type of cell with LLZO heat treated at 500 °C (Figures S15, S16 and Figure 6a, Table 4). X-ray photoelectron spectroscopy of the LLZO surface before and after the 700 °C heat treatment (Figure S17, Note S6) confirms that the treatment is an efficient method to remove Li_2CO_3 contamination from the surface of the LLZO. The reduction in the interfacial impedance at the PEO/LLZO interface using this heat treatment was further confirmed by EIS analysis of PEO/LLZO/PEO cells with blocking electrodes (Figure S18b,c), which demonstrated that the PEO/LLZO interface contributes little to the overall impedance at low frequencies when LLZO is treated at 700 °C. This result reveals that contamination at PEO/LLZO interfaces do not stem from reactions between these two

Table 4. Equivalent circuit values corresponding to the fit of the Nyquist plot of the Li//PEO/LLZO/PEO/Li cell at 80 °C shown in Figure 6a. Time constants calculated through $\tau = (QR)^{1/\alpha}$

Circuit element	Value	Units	RC time constant τ (s)	Assignment
R1	16.7	Ω cm^2	-	LLZO and PEO electrolyte resistances
R2	32.9	Ω cm^2	8.7×10^{-5}	Film resistances (Li/PEO and PEO/LLZO interfaces)
Q2	1.1×10^{-5}	F/cm^2		
$\alpha 2$	0.85	-		
R3	15.0	Ω cm^2	1.7×10^{-5}	Charge transfer at Li/PEO and PEO/LLZO interfaces
Q3	3.4×10^{-5}	F/cm^2		
$\alpha 3$	0.69	-		

materials as has been previously suggested, but rather from insufficient removal of native contamination on LLZO surfaces.

By minimizing the PEO/LLZO interfacial impedance, the Li/PEO interface becomes the most significant source of impedance in this cell, a conclusion which is consistent with the fact that the film resistance terms at 30 °C, as determined by EIS (~2800 Ω cm^2, Table S7) and by fitting of the CV curve (~2900 Ω cm^2), are quite close to the film resistance terms for Li/PEO cells at 30 °C (~2770 Ω cm^2, Table S1). Moreover, the largest peaks in the distribution of relaxation times (DRT) of both Li/PEO/LLZO/PEO/Li (Figure S18b, black curve) and Li/PEO/Li cells (Figure S6) are centered at the same relaxation time of ~$5.8 \cdot 10^{-3}$ s and can be assigned to the film resistance of the Li/PEO interface. Indeed, the assignment of this peak to the film resistance at the Li/PEO interface is supported by comparing the DRT of the Li/PEO/LLZO/PEO/Li cell with the DRT of the same type of cell but with stainless steel blocking electrodes (SS/PEO/LLZO/PEO/SS, Figure S18b, orange curve), which reveals that the film resistance peak disappears in the absence of Li/PEO interfaces. Notably, for this SS/PEO/LLZO/PEO/SS cell, the peak centered at $4.9 \cdot 10^{-4}$ s remains, corresponding to ion transfer at PEO/LLZO interfaces, which is further confirmed by a similar measured relaxation time assigned to ion transfer in the DRT of Li/LLZO/PEO/LLZO/Li cells ($4.1 \cdot 10^{-4}$ s, Figure S11b).

DC polarization measurements of the Li/PEO/LLZO/PEO/Li cells are nonlinear (Figure 6c, Figure S16d, Figure S18a), which is a result of the nonlinear kinetics of ion transfer at both Li/PEO and PEO/LLZO interfaces. Between 60 and 80 °C, the activation energy of the exchange current density as determined by EIS and CV is similar in magnitude (0.70 eV, Figure 6d) to the Li/PEO interface and the PEO/LLZO interface, as expected.

Given that the charge transfer reactions at the Li/PEO and PEO/LLZO interface occur at the same time scale, their individual impedance contributions intimately overlap in the EIS spectrum of the optimized Li/PEO/LLZO/PEO/Li cell, and cannot be separated on the basis of equivalent circuit modeling. That said, an upper bound estimate of the charge transfer resistance associated with ion transfer across the PEO/LLZO interface in this optimized cell can be made by subtracting the total interfacial resistance of a Li/PEO/Li cell at 30 °C (3005 Ω cm^2, Table S1) from the total interfacial resistance for the Li/PEO/LLZO/PEO/Li cell (3364 Ω cm^2, Table S7). Doing this yields an ion charge transfer resistance of 359 Ω cm^2 (~180 Ω cm^2 per PEO/LLZO interface), a value nearly equivalent to that reported by Gupta et al.[60] (180 Ω cm^2), and which translates to an exchange current density of 0.15 mA/cm^2. Figure 7 illustrates the comparison of charge transfer resistance and exchange current density for PEO/LLZO interfaces in this work to interfacial resistances and the corresponding exchange current densities reported for related PEO/ceramic electrolyte interfaces at 30 °C. Interfacial resistances at PEO/ceramic interfaces in these different systems span more than 1.5 orders of magnitude. While the variation in the actual charge transfer resistances at these interfaces may have some dependence on the identity of the lithium salt, salt concentration, and type of ceramic electrolyte, it is clear in this data set that the largest differentiating factor between these systems is the heat treatment of the ceramic electrolyte; the top three systems with the lowest interfacial resistances were all PEO/LLZO interfaces in which the LLZO was heat-treated. Thus, the trends shown in Figure 7 underscore the importance of controlling for surface chemistry at polymer/ceramic interfaces in order to reduce ion transport limitations through interfacial contamination layers.

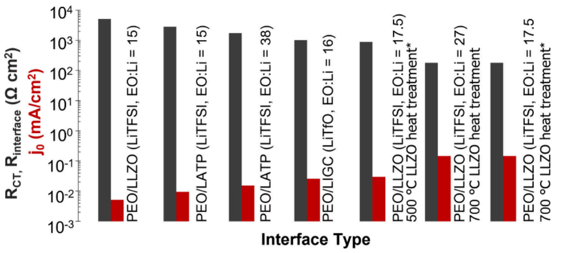

Figure 7. Reported values of interfacial resistance (gray bars) and the corresponding exchange current densities (red bars) at PEO/ceramic electrolyte interfaces at 30 °C. Exchange current density values from EIS were calculated by $j_0 = RT/FR_{int}$. Data were extracted from the following references, from left to right: 36, 36, 37, 63, *, 60, *. This work = *.

CONCLUSIONS

In this work, the architectures of multilayer solid-state batteries were systematically varied to investigate the charge transfer kinetics at Li/PEO and PEO/LLZO interfaces. By combining electrochemical impedance spectroscopy and DC polarization experiments with electrochemical kinetic analysis, we were able to quantitatively measure film resistances, charge transfer resistances, exchange current densities, and activation energies for interfacial charge transfer reactions at Li/PEO and PEO/LLZO interfaces. DC polarization measurements reveal the nonlinear nature of ion transfer kinetics between at the PEO/LLZO interface. The magnitudes of the exchange current densities, the activation energies, and the time scale of charge transfer reactions were found to be similar for Li/PEO and PEO/LLZO interfaces, suggesting that the Li/PEO charge transfer reaction is limited by ion transfer, rather than electron transfer. Additionally, it was found that ion transport through interfacial layers at (SEI at Li/PEO interfaces and contamination layers at PEO/LLZO interfaces) are major sources of impedance, more so than charge transfer resistances. For PEO/LLZO interfaces, such ion transport limitations can be overcome by proper heat treatment of the LLZO electrolyte, leaving ion transport through the SEI at the Li/PEO interface as the dominant source of impedance in multilayer Li/PEO/LLZO/PEO/Li cells. Thus, in order to take advantage of the high conductivity of LLZO to boost the total conductivity of traditional composite electrolytes, heat treatments combined with the strict prevention of exposure to air and/or solvents that damage contamination-prone LLZO surfaces are imperative. Furthermore, improvements must be made through interfacial engineering of Li/polymer interfaces to reduce ohmic losses due to ion transport through SEI films.

AUTHOR INFORMATION

Corresponding Author

Yang Shao-Horn − *Department of Materials Science and Engineering, Massachusetts Institute of Technology, Cambridge, Massachusetts 02139, United States; Research Laboratory of Electronics and Department of Mechanical Engineering, Massachusetts Institute of Technology, Cambridge, Massachusetts 02139, United States;* orcid.org/0000-0001-8714-2121; Email: shaohorn@mit.edu

Authors

Bryce A. Tappan − *Research Laboratory of Electronics, Massachusetts Institute of Technology, Cambridge, Massachusetts 02139, United States;* orcid.org/0000-0002-9776-6445

Katrin Geng − *Karlsruhe Institute of Technology (KIT), 76021 Karlsruhe, Germany; Helmholtz Institute Ulm (HIU), 89081 Ulm, Germany;* orcid.org/0000-0003-4347-4225

Daniele Vivona − *Department of Materials Science and Engineering, Massachusetts Institute of Technology, Cambridge, Massachusetts 02139, United States*

Daniel Wang − *Department of Mechanical Engineering, Massachusetts Institute of Technology, Cambridge, Massachusetts 02139, United States*

David Mankus − *Koch Institute for Integrative Cancer Research, Massachusetts Institute of Technology, Cambridge, Massachusetts 02139, United States;* orcid.org/0000-0002-9979-7608

Abigail Lytton-Jean − *Koch Institute for Integrative Cancer Research, Massachusetts Institute of Technology, Cambridge, Massachusetts 02139, United States;* orcid.org/0000-0002-1582-0066

Dominic Bresser − *Karlsruhe Institute of Technology (KIT), 76021 Karlsruhe, Germany; Helmholtz Institute Ulm (HIU), 89081 Ulm, Germany;* orcid.org/0000-0001-6429-6048

Author Contributions

B.T. and Y.S.-H. conceived the idea. B.T. performed material synthesis, electrochemical testing, room-temperature SEM, XRD, NMR, and data analysis. K.G. contributed to data interpretation, DRT analysis, and to the design of experiments. B.T. wrote the manuscript under supervision of Y.S.-H. with edits, revisions, and scientific discussions also provided by D.V., K.G., and D.B. XPS measurements were carried out by D.W. Cryo-SEM was carried out with the help of D.M. and A.L.-J. The authors declare no competing interests.

Author Contributions

°K.G. and D.V. contributed equally

Notes

The authors declare no competing financial interest.

ACKNOWLEDGMENTS

This work was supported by funding from the NASA Ames Research Center through award number 80NSSC21M0108. The authors gratefully acknowledge the financial support by the German Federal Ministry of Education and Research (BMBF) within the LISI-2 project (03XP0509D). Cryo-SEM analysis was supported in part by the Koch Institute Support (core) Grant P30-CA14051 from the National Cancer Institute. We thank the Koch Institute's Robert A. Swanson (1969) Biotechnology Center for technical support, specifically Nanotechnology Materials core (RRID:SCR_018674) for cryo-SEM analysis. We thank Dr. Bruce Adams for assistance with solid-state NMR, and MIT DCIF for use of NMR facilities.

REFERENCES

(1) Janek, J.; Zeier, W. G. A Solid Future for Battery Development. *Nat. Energy* **2016**, *1* (9), 1−4.

(2) Betz, J.; Bieker, G.; Meister, P.; Placke, T.; Winter, M.; Schmuch, R. Theoretical versus Practical Energy: A Plea for More Transparency in the Energy Calculation of Different Rechargeable Battery Systems. *Adv. Energy Mater.* **2019**, *9* (6), 1803170.

(3) Krauskopf, T.; Richter, F. H.; Zeier, W. G.; Janek, J. Physicochemical Concepts of the Lithium Metal Anode in Solid-State Batteries. *Chem. Rev.* **2020**, *120* (15), 7745−7794.

(4) Xue, W.; Huang, M.; Li, Y.; Zhu, Y. G.; Gao, R.; Xiao, X.; Zhang, W.; Li, S.; Xu, G.; Yu, Y.; Li, P.; Lopez, J.; Yu, D.; Dong, Y.; Fan, W.; Shi, Z.; Xiong, R.; Sun, C.-J.; Hwang, I.; Lee, W.-K.; Shao-Horn, Y.; Johnson, J. A.; Li, J. Ultra-High-Voltage Ni-Rich Layered Cathodes in Practical Li Metal Batteries Enabled by a Sulfonamide-Based Electrolyte. *Nat. Energy* **2021**, *6* (5), 495−505.

(5) Niu, C.; Liu, D.; Lochala, J. A.; Anderson, C. S.; Cao, X.; Gross, M. E.; Xu, W.; Zhang, J.-G.; Whittingham, M. S.; Xiao, J.; Liu, J. Balancing Interfacial Reactions to Achieve Long Cycle Life in High-Energy Lithium Metal Batteries. *Nat. Energy* **2021**, *6* (7), 723−732.

(6) Krauskopf, T.; Mogwitz, B.; Hartmann, H.; Singh, D. K.; Zeier, W. G.; Janek, J. The Fast Charge Transfer Kinetics of the Lithium Metal Anode on the Garnet-Type Solid Electrolyte Li6.25Al0.25La3Zr2O12. *Adv. Energy Mater.* **2020**, *10* (27), 2000945.

(7) Han, X.; Gong, Y.; Fu, K.; He, X.; Hitz, G. T.; Dai, J.; Pearse, A.; Liu, B.; Wang, H.; Rubloff, G.; Mo, Y.; Thangadurai, V.; Wachsman, E. D.; Hu, L. Negating Interfacial Impedance in Garnet-Based Solid-State Li Metal Batteries. *Nat. Mater.* **2017**, *16* (5), 572−579.

(8) Hitz, G. T.; McOwen, D. W.; Zhang, L.; Ma, Z.; Fu, Z.; Wen, Y.; Gong, Y.; Dai, J.; Hamann, T. R.; Hu, L.; Wachsman, E. D. High-Rate Lithium Cycling in a Scalable Trilayer Li-Garnet-Electrolyte Architecture. *Mater. Today* **2019**, *22*, 50−57.

(9) Krauskopf, T.; Hartmann, H.; Zeier, W. G.; Janek, J. Toward a Fundamental Understanding of the Lithium Metal Anode in Solid-State Batteries—An Electrochemo-Mechanical Study on the Garnet-Type Solid Electrolyte Li6.25Al0.25La3Zr2O12. *ACS Appl. Mater. Interfaces* **2019**, *11* (15), 14463−14477.

(10) Hobold, G. M.; Lopez, J.; Guo, R.; Minafra, N.; Banerjee, A.; Shirley Meng, Y.; Shao-Horn, Y.; Gallant, B. M. Moving beyond 99.9%

Coulombic Efficiency for Lithium Anodes in Liquid Electrolytes. *Nat. Energy* **2021**, *6* (10), 951−960.

(11) Fauteux, D. Lithium Electrode in Polymer Electrolytes. *Electrochim. Acta* **1993**, *38* (9), 1199−1210.

(12) Sequeira, C. A. C.; Hooper, A. The Study of Lithium Electrode Reversibility against (PEO)XLiF3CSO3 Polymeric Electrolytes. *Solid State Ion.* **1983**, *9*−*10*, 1131−1138.

(13) Kinzer, B.; Davis, A. L.; Krauskopf, T.; Hartmann, H.; LePage, W. S.; Kazyak, E.; Janek, J.; Dasgupta, N. P.; Sakamoto, J. Operando Analysis of the Molten Li|LLZO Interface: Understanding How the Physical Properties of Li Affect the Critical Current Density. *Matter* **2021**, *4* (6), 1947−1961.

(14) Lewis, J. A.; Cortes, F. J. Q.; Liu, Y.; Miers, J. C.; Verma, A.; Vishnugopi, B. S.; Tippens, J.; Prakash, D.; Marchese, T. S.; Han, S. Y.; Lee, C.; Shetty, P. P.; Lee, H.-W.; Shevchenko, P.; De Carlo, F.; Saldana, C.; Mukherjee, P. P.; McDowell, M. T. Linking Void and Interphase Evolution to Electrochemistry in Solid-State Batteries Using Operando X-Ray Tomography. *Nat. Mater.* **2021**, *20* (4), 503−510.

(15) Banerjee, A.; Wang, X.; Fang, C.; Wu, E. A.; Meng, Y. S. Interfaces and Interphases in All-Solid-State Batteries with Inorganic Solid Electrolytes. *Chem. Rev.* **2020**, *120* (14), 6878−6933.

(16) Kasemchainan, J.; Zekoll, S.; Spencer Jolly, D.; Ning, Z.; Hartley, G. O.; Marrow, J.; Bruce, P. G. Critical Stripping Current Leads to Dendrite Formation on Plating in Lithium Anode Solid Electrolyte Cells. *Nat. Mater.* **2019**, *18* (10), 1105−1111.

(17) Eckhardt, J. K.; Klar, P. J.; Janek, J.; Heiliger, C. Interplay of Dynamic Constriction and Interface Morphology between Reversible Metal Anode and Solid Electrolyte in Solid State Batteries. *ACS Appl. Mater. Interfaces* **2022**, *14* (31), 35545−35554.

(18) Din, M. M. U.; Häusler, M.; Fischer, S. M.; Ratzenböck, K.; Chamasemani, F. F.; Hanghofer, I.; Henninge, V.; Brunner, R.; Slugovc, C.; Rettenwander, D. Role of Filler Content and Morphology in LLZO/PEO Membranes. *Front. Energy Res.* **2021**, *9*, 711610.

(19) Chen, F.; Yang, D.; Zha, W.; Zhu, B.; Zhang, Y.; Li, J.; Gu, Y.; Shen, Q.; Zhang, L.; Sadoway, D. R. Solid Polymer Electrolytes Incorporating Cubic Li7La3Zr2O12 for All-Solid-State Lithium Rechargeable Batteries. *Electrochim. Acta* **2017**, *258*, 1106−1114.

(20) Yao, P.; Yu, H.; Ding, Z.; Liu, Y.; Lu, J.; Lavorgna, M.; Wu, J.; Liu, X. Review on Polymer-Based Composite Electrolytes for Lithium Batteries. *Front. Chem.* **2019**, *7*, 522.

(21) Yang, L.; Wang, Z.; Feng, Y.; Tan, R.; Zuo, Y.; Gao, R.; Zhao, Y.; Han, L.; Wang, Z.; Pan, F. Flexible Composite Solid Electrolyte Facilitating Highly Stable "Soft Contacting" Li-Electrolyte Interface for Solid State Lithium-Ion Batteries. *Adv. Energy Mater.* **2017**, *7* (22), 1701437.

(22) Lennartz, P.; Paren, B. A.; Herzog-Arbeitman, A.; Chen, X. C.; Johnson, J. A.; Winter, M.; Shao-Horn, Y.; Brunklaus, G. Practical Considerations for Enabling Li|polymer Electrolyte Batteries. *Joule* **2023**, *7* (7), 1471−1495.

(23) Bachman, J. C.; Muy, S.; Grimaud, A.; Chang, H.-H.; Pour, N.; Lux, S. F.; Paschos, O.; Maglia, F.; Lupart, S.; Lamp, P.; Giordano, L.; Shao-Horn, Y. Inorganic Solid-State Electrolytes for Lithium Batteries: Mechanisms and Properties Governing Ion Conduction. *Chem. Rev.* **2016**, *116* (1), 140−162.

(24) Berliner, M. D.; McGill, B. C.; Majeed, M.; Hallinan, D. T. Electrochemical Kinetics of Lithium Plating and Stripping in Solid Polymer Electrolytes: Pulsed Voltammetry. *J. Electrochem. Soc.* **2019**, *166* (2), A297.

(25) Blume, L.; Sauter, U.; Jacob, T. Non-Linear Kinetics of the Lithium-Solid Polymer Electrolyte Interface. *Electrochim. Acta* **2019**, *318*, 551−559.

(26) Long, L.; Wang, S.; Xiao, M.; Meng, Y. Polymer Electrolytes for Lithium Polymer Batteries. *J. Mater. Chem. A* **2016**, *4* (26), 10038−10069.

(27) Zhao, Y.; Wang, L.; Zhou, Y.; Liang, Z.; Tavajohi, N.; Li, B.; Li, T. Solid Polymer Electrolytes with High Conductivity and Transference Number of Li Ions for Li-Based Rechargeable Batteries. *Adv. Sci.* **2021**, *8* (7), 2003675.

(28) Chen, L.; Li, Y.; Li, S.-P.; Fan, L.-Z.; Nan, C.-W.; Goodenough, J. B. PEO/Garnet Composite Electrolytes for Solid-State Lithium Batteries: From "Ceramic-in-Polymer" to "Polymer-in-Ceramic.". *Nano Energy* **2018**, *46*, 176−184.

(29) Gupta, A.; Kazyak, E.; Dasgupta, N. P.; Sakamoto, J. Electrochemical and Surface Chemistry Analysis of Lithium Lanthanum Zirconium Tantalum Oxide (LLZTO)/Liquid Electrolyte (LE) Interfaces. *J. Power Sources* **2020**, *474*, 228598.

(30) Sharafi, A.; Kazyak, E.; Davis, A. L.; Yu, S.; Thompson, T.; Siegel, D. J.; Dasgupta, N. P.; Sakamoto, J. Surface Chemistry Mechanism of Ultra-Low Interfacial Resistance in the Solid-State Electrolyte Li7La3Zr2O12. *Chem. Mater.* **2017**, *29* (18), 7961−7968.

(31) Zhu, Y.; Connell, J. G.; Tepavcevic, S.; Zapol, P.; Garcia-Mendez, R.; Taylor, N. J.; Sakamoto, J.; Ingram, B. J.; Curtiss, L. A.; Freeland, J. W.; Fong, D. D.; Markovic, N. M. Dopant-Dependent Stability of Garnet Solid Electrolyte Interfaces with Lithium Metal. *Adv. Energy Mater.* **2019**, *9* (12), 1803440.

(32) Cheng, L.; Crumlin, E. J.; Chen, W.; Qiao, R.; Hou, H.; Lux, S. F.; Zorba, V.; Russo, R.; Kostecki, R.; Liu, Z.; Persson, K.; Yang, W.; Cabana, J.; Richardson, T.; Chen, G.; Doeff, M. The Origin of High Electrolyte-Electrode Interfacial Resistances in Lithium Cells Containing Garnet Type Solid Electrolytes. *Phys. Chem. Chem. Phys.* **2014**, *16* (34), 18294−18300.

(33) Keller, M.; Varzi, A.; Passerini, S. Hybrid Electrolytes for Lithium Metal Batteries. *J. Power Sources* **2018**, *392*, 206−225.

(34) Zhou, W.; Wang, S.; Li, Y.; Xin, S.; Manthiram, A.; Goodenough, J. B. Plating a Dendrite-Free Lithium Anode with a Polymer/Ceramic/Polymer Sandwich Electrolyte. *J. Am. Chem. Soc.* **2016**, *138* (30), 9385−9388.

(35) Li, Y.; Xu, B.; Xu, H.; Duan, H.; Lü, X.; Xin, S.; Zhou, W.; Xue, L.; Fu, G.; Manthiram, A.; Goodenough, J. B. Hybrid Polymer/Garnet Electrolyte with a Small Interfacial Resistance for Lithium-Ion Batteries. *Angew. Chem., Int. Ed.* **2017**, *56* (3), 753−756.

(36) Trevisanello, E.; Ates, T.; Passerini, S.; Richter, F. H.; Janek, J. Influence of the Polymer Structure and Its Crystallization on the Interface Resistance in Polymer-LATP and Polymer-LLZO Hybrid Electrolytes. *J. Electrochem. Soc.* **2022**, *169* (11), 110547.

(37) Isaac, J. A.; Mangani, L. R.; Devaux, D.; Bouchet, R. Electrochemical Impedance Spectroscopy of PEO-LATP Model Multilayers: Ionic Charge Transport and Transfer. *ACS Appl. Mater. Interfaces* **2022**, *14* (11), 13158−13168.

(38) Li, Y.; Han, J.-T.; Wang, C.-A.; Xie, H.; Goodenough, J. B. Optimizing Li + Conductivity in a Garnet Framework. *J. Mater. Chem.* **2012**, *22* (30), 15357−15361.

(39) Fauteux, D. Formation of a Passivating Film at the Lithium-PEO-LiCF3SO3 Interface. *Solid State Ion.* **1985**, *17* (2), 133−138.

(40) Fauteux, D. Lithium Electrode/PEO-Based Polymer Electrolyte Interface Behavior Between 60° and 120°C. *J. Electrochem. Soc.* **1988**, *135* (9), 2231.

(41) Sharafi, A.; Meyer, H. M.; Nanda, J.; Wolfenstine, J.; Sakamoto, J. Characterizing the Li-Li7La3Zr2O12 Interface Stability and Kinetics as a Function of Temperature and Current Density. *J. Power Sources* **2016**, *302*, 135−139.

(42) MaximeVH. DRT.Jl, 2023. https://github.com/MaximeVH/DRT.jl (accessed 2023−11−12).

(43) Kataoka, K.; Akimoto, J. Lithium-Ion Conductivity and Crystal Structure of Garnet-Type Solid Electrolyte $Li_{7-x}La_3Zr_{2-x}Ta_xO_{12}$ Using Single-Crystal. *J. Ceram. Soc. Jpn.* **2019**, *127* (8), 521−526.

(44) Fairley, N.; Fernandez, V.; Richard-Plouet, M.; Guillot-Deudon, C.; Walton, J.; Smith, E.; Flahaut, D.; Greiner, M.; Biesinger, M.; Tougaard, S.; Morgan, D.; Baltrusaitis, J. Systematic and Collaborative Approach to Problem Solving Using X-Ray Photoelectron Spectroscopy. *Appl. Surf. Sci. Adv.* **2021**, *5*, 100112.

(45) Bouchet, R.; Lascaud, S.; Rosso, M. An EIS Study of the Anode Li/PEO-LiTFSI of a Li Polymer Battery. *J. Electrochem. Soc.* **2003**, *150* (10), A1385.

(46) Ushakova, E. E.; Frolov, A.; Reveguk, A. A.; Usachov, D. Yu.; Itkis, D. M.; Yashina, L. V. Solid Electrolyte Interface Formation

between Lithium and PEO-Based Electrolyte. *Appl. Surf. Sci.* **2022**, *589*, 153014.

(47) Andersson, E. K. W.; Sångeland, C.; Berggren, E.; Johansson, F. O. L.; Kühn, D.; Lindblad, A.; Mindemark, J.; Hahlin, M. Early-Stage Decomposition of Solid Polymer Electrolytes in Li-Metal Batteries. *J. Mater. Chem. A* **2021**, *9* (39), 22462−22471.

(48) Wu, L.-T.; Nachimuthu, S.; Brandell, D.; Jiang, J.-C. Prediction of SEI Formation in All-Solid-State Batteries: Computational Insights from PCL-Based Polymer Electrolyte Decomposition on Lithium-Metal. *Batter. Supercaps* **2022**, *5* (9), No. e202200088.

(49) Sheng, O.; Zheng, J.; Ju, Z.; Jin, C.; Wang, Y.; Chen, M.; Nai, J.; Liu, T.; Zhang, W.; Liu, Y.; Tao, X. In Situ Construction of a LiF-Enriched Interface for Stable All-Solid-State Batteries and Its Origin Revealed by Cryo-TEM. *Adv. Mater.* **2020**, *32* (34), 2000223.

(50) Jagger, B.; Pasta, M. Solid Electrolyte Interphases in Lithium Metal Batteries. *Joule* **2023**, *7* (10), 2228−2244.

(51) Smith, R. B.; Bazant, M. Z. Multiphase Porous Electrode Theory. *J. Electrochem. Soc.* **2017**, *164* (11), No. E3291.

(52) Doyle, M.; Newman, J.; Gozdz, A. S.; Schmutz, C. N.; Tarascon, J.-M. Comparison of Modeling Predictions with Experimental Data from Plastic Lithium Ion Cells. *J. Electrochem. Soc.* **1996**, *143* (6), 1890.

(53) Marzantowicz, M.; Dygas, J. R.; Krok, F.; Łasińska, A.; Florjańczyk, Z.; Zygadło-Monikowska, E.; Affek, A. Crystallization and Melting of PEO:LiTFSI Polymer Electrolytes Investigated Simultaneously by Impedance Spectroscopy and Polarizing Microscopy. *Electrochim. Acta* **2005**, *50* (19), 3969−3977.

(54) Dhivya, L.; Janani, N.; Palanivel, B.; Murugan, R. Li+ Transport Properties of W Substituted Li7La3Zr2O12 Cubic Lithium Garnets. *AIP Adv.* **2013**, *3* (8), 082115.

(55) Tenhaeff, W. E.; Rangasamy, E.; Wang, Y.; Sokolov, A. P.; Wolfenstine, J.; Sakamoto, J.; Dudney, N. J. Resolving the Grain Boundary and Lattice Impedance of Hot-Pressed Li7La3Zr2O12 Garnet Electrolytes. *ChemElectroChem.* **2014**, *1* (2), 375−378.

(56) Krauskopf, T.; Mogwitz, B.; Rosenbach, C.; Zeier, W. G.; Janek, J. Diffusion Limitation of Lithium Metal and Li-Mg Alloy Anodes on LLZO Type Solid Electrolytes as a Function of Temperature and Pressure. *Adv. Energy Mater.* **2019**, *9* (44), 1902568.

(57) Posch, P.; Lunghammer, S.; Berendts, S.; Ganschow, S.; Redhammer, G. J.; Wilkening, A.; Lerch, M.; Gadermaier, B.; Rettenwander, D.; Wilkening, H. M. R. Ion Dynamics in Al-Stabilized Li7La3Zr2O12 Single Crystals - Macroscopic Transport and the Elementary Steps of Ion Hopping. *Energy Storage Mater.* **2020**, *24*, 220−228.

(58) Abe, T.; Ohtsuka, M.; Sagane, F.; Iriyama, Y.; Ogumi, Z. Lithium Ion Transfer at the Interface between Lithium-Ion-Conductive Solid Crystalline Electrolyte and Polymer Electrolyte. *J. Electrochem. Soc.* **2004**, *151* (11), A1950.

(59) Langer, F.; Palagonia, M. S.; Bardenhagen, I.; Glenneberg, J.; La Mantia, F.; Kun, R. Impedance Spectroscopy Analysis of the Lithium Ion Transport through the Li7La3Zr2O12/P(EO)20Li Interface. *J. Electrochem. Soc.* **2017**, *164* (12), A2298.

(60) Gupta, A.; Sakamoto, J. Controlling Ionic Transport through the PEO-LiTFSI/LLZTO Interface. *Electrochem. Soc. Interface* **2019**, *28* (2), 63.

(61) Ghorbanzade, P.; Pesce, A.; Gómez, K.; Accardo, G.; Devaraj, S.; López-Aranguren, P.; López del Amo, J. M. Impact of Thermal Treatment on the Li-Ion Transport, Interfacial Properties, and Composite Preparation of LLZO Garnets for Solid-State Electrolytes. *J. Mater. Chem. A* **2023**, *11* (22), 11675−11683.

(62) Ghorbanzade, P.; Accardo, G.; Gomez, K.; López-Aranguren, P.; Devaraj, S.; Costa, C. M.; Lanceros-Mendez, S.; López del Amo, J. M. Influence of the LLZO-PEO Interface on the Micro- and Macroscale Properties of Composite Polymer Electrolytes for Solid-State Batteries. *Mater. Today Energy* **2023**, *38*, 101448.

(63) Chen, X. C.; Liu, X.; Samuthira Pandian, A.; Lou, K.; Delnick, F. M.; Dudney, N. J. Determining and Minimizing Resistance for Ion Transport at the Polymer/Ceramic Electrolyte Interface. *ACS Energy Lett.* **2019**, *4* (5), 1080−1085.